Applied Thermal Engineering 255 (2024) 124044

Contents lists available at ScienceDirect

Applied Thermal Engineering

journal homepage: www.elsevier.com/locate/apthermeng

Research Paper

Design solutions and characterization of a small scale and very high concentration solar furnace using a Fresnel lens

Héctor González-Camarillo [a], Alessandro Gallo [b,c,*], Isabel Padilla [d,*], Carlos A. Pérez-Rábago [a], Charles-Alexis Asselineau [e,f], Maximina Romero [d], Aurora López-Delgado [d]

[a] *Institute of Renewable Energy, National Autonomous University of Mexico (IER-UNAM), Priv. Xochicalco S/N, Temixco 62580, Morelos, Mexico*
[b] *University of Almeria, Carretera Sacramento S/N, 04120 La Cañada de San Urbano, 04120 Almeria, Spain*
[c] *Carlos III University of Madrid, School of Engineering, Department of Thermal and Fluid Engineering, Energy Systems Engineering Group (ISE), Av. Universidad 30, 28911, Leganes, Madrid, Spain*
[d] *MEDES-IETcc Group. Eduardo Torroja Institute for Construction Sciences, IETcc-CSIC, C/ Serrano Galvache, 4, 28033 Madrid, Spain*
[e] *School of Engineering, The Australian National University, ACT 2601, Australia*
[f] *Polytechnic University of Madrid, School of Industrial Engineering, Department of Energy Engineering, José Gutiérrez Abascal 2, 28006 Madrid, Spain*

ARTICLE INFO

Keywords:
Fresnel lens
Material synthesis
Solar furnace
High-temperature processes
Concentrated Solar Energy

ABSTRACT

The use of Fresnel lenses for solar energy concentration technology dates back to the 1950 s. These lenses feature a plano-convex optical design with a series of discontinuous convex grooves. Typically made from materials like polymethyl methacrylate, Fresnel lenses are lightweight, resistant to sunlight, thermally stable, and cost-effective.

This study presents a novel Fresnel lens-based solar furnace configuration installed at the Eduardo Torroja Institute for Construction Science in Madrid, Spain. The novelty of this work lies in the exceptional performance and operability of the facility. Experimental characterization revealed a record peak irradiance over 7 MW m^{-2} for an incident target power exceeding 800 W. Comparison with ray tracing simulations shows good agreement with experimental results. This setup enables high temperature experiments up to 2000 °C with rapid execution times. A fixed receiver, a shutter system and a closed-loop heliostat tracking control system allow for flexible operation up to 5000 suns and straightforward maintenance. The concentrator element costs less than 300 USD (2022) m^{-2}, offering an economical solution to solar-powered high concentration and temperature applications. This innovative design overcomes previous operational challenges, providing a robust and economical method for high-temperature material processing and other industrial applications.

1. Introduction

Research into alternative energy sources plays a crucial role in the industrial decarbonization. Concentrating solar technologies (CST) can reduce the environmental impact of numerous processes that require heat across a broad temperature spectrum, from just above ambient temperatures to several thousand degrees Celsius [1,2].

Examples of CST include parabolic trough collectors, linear Fresnel collectors with or without beam-down optics, solar towers, solar furnaces, compound parabolic concentrators and Fresnel lenses (FL) technologies [3–9]. This work is focused on the FL technology that, in contrast to other technologies, relies on refractive optics rather than mirrors.

FL based CST dates back to the 1950 s [10]. FLs exhibit a plano-convex optical design, where the curvature of the lens is split into a series of thinner, discontinuous grooves resulting in lower weight, smaller volume, lower light attenuation and therefore significantly increase energy density when compared to non-Fresnel-based designs [11]. FLs can be designed as line or point focus concentrators. Point focus FLs can generate very high fluxes and consequently very high temperatures in compact installations that require minimal maintenance [8].

FLs are typically made of transparent materials such as glass, silicon on glass or polymethyl methacrylate (PMMA), also known as “acrylic”. PMMA is the most used material because of its favourable properties: lightweight, resistant to UV degradation, thermally stable up to 80 °C,

---

* Corresponding authors.
E-mail addresses: algallo@ing.uc3m.es (A. Gallo), isabel.padilla@ietcc.csic.es (I. Padilla).

https://doi.org/10.1016/j.applthermaleng.2024.124044
Received 13 April 2024; Received in revised form 23 July 2024; Accepted 25 July 2024

high transmittance in the solar spectrum with an average refractive index of 1.49, and ease of manufacture into complex shapes with high precision. PMMA FLs exist in a wide range of sizes, typically limited by manufacturing capabilities and FLs are relatively low cost [10,12–14]. The price of 1 m^2 of a PMMA FL ranges from 100 to 600 USD (2004–2021) [12,15,16]. For continuous receiver operations, the FL must be mounted on a tracking system. The tracker can be manual or automatic. In the latter case, Cañadilla et al. estimate the total cost of the facility, with a 1 m^2 lens (costing around 600 USD), tracker, control system, etc., to 7000 USD (2021) [15].

Solar FLs exhibit remarkable versatility for a wide variety of applications, including solar cooking, water heating, concentrated photovoltaics (CPV), metallurgy, sintering of materials, biofuel production, solar pyrolysis, solar desalination and solar pumped laser, among others [12,15,17–26].

In the field of CPV, FLs have been coupled with multijunction cells to enhance efficiency compared to traditional silicon cells [27]. CPV concentration factors range from a few to hundreds of suns, necessitating accurate dual-axis tracking that increases costs [13,28–30]. Spectral variations of the refractive index of PMMA result in spectral dispersion and ultimately chromatic aberrations which are important for CPV systems efficiency [31]. Strong spatial variations of flux are also detrimental to CPV efficiency and secondary concentrators, including non-imaging optic concentrators, are often used [19,30,32]. In thermophotovoltaic applications, Andreev et al. reported a concentration factor of approximately 4000 suns achieved by adding a secondary quartz meniscus lens to enhance receiver concentration [33].

Numerous thermal and thermochemical applications of FLs have been reported in the literature. At the Institute of Chemical Technology in Matunga, India, a square FL (0.3 m side) with a manual tracking was used for low temperature (below 100 °C) synthesis of palladium and silver nanoparticles and biodiesel production [34–38]. Michalsky and Pfromm used a FL (0.93 m by 1.024 m, 7 mm thickness, focal length of 1.03 m) for the synthesis of ammonia through a thermochemical cycle using metallic chromium and nitrogen as reactants at high temperatures (up to 1600 °C). The lens achieved a maximum concentration factor of 2440 suns with manual tracking [39]. Other FL facilities exist in Mexico, Brazil, Lebanon and USA [20,25,26,39]. In Spain, at the University of Castilla La Mancha a circular FL (0.9 m diameter, 0.0317 m thickness, focal length of 0.757 m, groove pitch of 0.5 mm) was mounted on a two-axis automatic tracking system and used for high temperature sintering of different metals, such as steel or aluminum [15,40,41]. This lens was optically characterized at CNRS-IMP in Odeillo and was shown to concentrate solar radiation with a Gaussian shape achieving an irradiance peak of 2644 suns [16]. An identical FL was installed at CENIM-CSIC on an equatorial mount that consisted of an automatic single-axis polar tracker while the elevation was manually adjusted to keep the lens always facing the Sun [42]. Morris et al. [21] and Mazo et al. [43] studied materials for high-temperature applications, exposing them to thermal shock tests, heated to 1200 °C at the highest heating rate. The same FL was also used to produce alumina [44] and dehydrate gypsum [45], reaching operating temperatures of over 1200 °C in less than a minute, and to evaluate different ceramic materials for use in solar receivers [46].

Mounting both a FL and a receiver on a solar tracker can result in two main drawbacks. First, tracking system inaccuracies can cause significant efficiency loss, an effect more prevalent in manual tracking systems. To address this issue, Zeaiter et al. designed and tested a FL mounted on a closed-loop two-axis tracking system based on the feedback signal from six frame-mounted photo-resistors that resulted in improved tracking accuracy for catalytic pyrolysis of scrap rubber tires at 550 °C [20,47]. Second, positioning, immobilization and instrumentation of samples in a moving receiver system with an open aperture can be complex, notably for high-temperature experiments. Both issues can be remedied by adopting a solar furnace configuration in which an automated heliostat redirects solar radiation towards a fixed FL that concentrates energy onto a fixed receiver. This arrangement facilitates the installation of a shutter to control the amount of radiation transmitted. Recently, Estremera-Pedriza et al. tested this configuration at Plataforma Solar de Almería, achieving an irradiance peak of 1134 kW m^{-2} (maximum concentration factor of 1300 suns) and a total power of 1.24 kW [48]. Similarly, Zhao et al. tested a FL-based solar furnace (focal length 0.3 m, groove pitch 1 mm) reaching a concentration factor of approximately 600 suns [49].

In this study, the design and characterization of a novel FL-based solar furnace with the following requirements is presented:

1. High flexibility to operate with different receivers/reactors and perform processes for diverse applications.
2. 2000 °C maximum operation temperature.
3. Modulable radiative flux from tens to several thousands of suns, enabling the execution of both slow processes with controlled heating and processes with short run times and fast thermal ramps.

The energy and optical performance of the facility are determined experimentally and verified against theoretical predictions using an open-source ray-tracing model. Key parameters such as the exact focal position, the lens concentration factor, the power on the receiver, the shutter behavior, and the maximum achievable temperature are estimated. While several innovations are presented, the main novelty of this work resides in the experimental demonstration of a system with significantly higher optical performance than previously reported at a relatively low-cost.

2. Methodology

2.1. Facility description

The main components of this FL-based solar furnace include a heliostat, a static FL, a shutter, and a receiver. The heliostat redirects the solar radiation (R_i) through the FL (R_{rh}), which concentrates the radiation (R_{rf}) onto the receiver. A webcam is positioned in front of the heliostat to provide a feedback signal for the closed-loop control system and optimize the mirror's alignment with the lens. A schematic representation of the solar furnace illustrating its main components and dimensions is presented in Fig. 1.

The heliostat supports a single flat and square-shaped facet of 1.5 m side length (l_h) with a solar-weighted reflectance (ρ_h) of 0.94 and two linear actuators. The heliostat was oversized to ensure full irradiation of the FL from 10 a.m. to 2p.m. (solar hours).

The solar tracking system combines an open-loop and a closed-loop control strategy. The open-loop control is based on the solar positioning algorithm proposed by Reda and Andreas [50] implemented in a real-time control device with configurable inputs and outputs. This controller sends signals corresponding to the angles obtained by the algorithm to the linear actuators of the elevation and tilt axes, maintaining the incident radiation on the FL during operations. The heliostat position control in both axes is performed by an accelerometer integrated in the main controller and mounted on the heliostat mirror support structure. A webcam placed in front of the heliostat mirror observes the position of the sun as reflected by the mirror (XY centroid) and provides feedback to refine the open-loop control via a closed-loop strategy (see Figs. 1 and 2b). Deviation between the theoretical and observed sun positions (using a fixed reference in the image) is used to determine the tracking error. With this error, the correction angles for both axes are obtained and sent to the linear actuators [51].

The Fresnel lens used is made of PMMA and is square with a side length (h_f) of 1.1 m and a base thickness of 5 mm. The focal length (f) is approximately 1 m and the transmittance (τ_l) of the lens is 0.92 according to the provider. The f-number (ratio of f to the lens diagonal) is 0.643. The manufacturer did not provide detailed geometrical profile

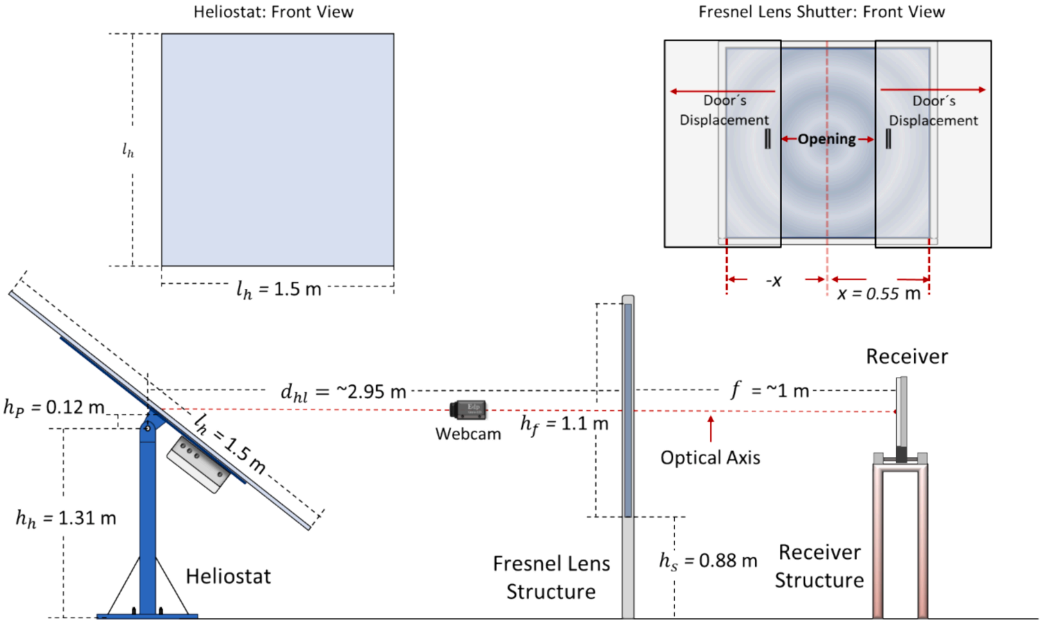

Fig. 1. Layout of the FL-based solar furnace system (dimensions and distances are not scaled).

data, however, visual inspection showed that the lens is composed of 2200 axisymmetric grooves with a fixed step width of 0.5 mm. The height of the grooves varies along the profile to obtain the necessary angle to refract light towards the focal point. This element costs 350 USD (2022) [52] which is significantly cheaper than typical reflective paraboloid concentrators [53].

The shutter consists of four sliding doors, two on either side of the lens, that have the twofold function of modulating the radiation received on the target and protecting the lens by closing the doors when the facility is not in use.

The receiver is located at the focal point of the FL for maximum flux operations.

2.2. Experimental setup

Optical characterization is obtained using the standard camera-image instrumentation, also known as Beam Characterization System (BCS) when applied to heliostat fields [54]. A water-cooled target, consisting of two joined rectangular aluminum plates (0.2 x 0.3 m), was used as a pseudo-Lambertian surface (see Fig. 2a and b). The front face of the Lambertian target was first subjected to sandblasting to uniformly roughen the surface and remove contaminants. The surface was then cleaned with water and painted with a white varnish (commercial high-temperature spray paint). A water-cooled Gardon-type radiometer (Vatell TG-1000–1) was inserted through a one-inch diameter hole in the target plates. The radiometer was connected to a Data Acquisition (DAQ) system (National Instrument USB-9162) for continuous irradiance recording. A CCD camera (Basler scA 1300–32 gm) was fixed to the target assembly and aimed back at the characterization target surface to obtain irradiance distribution maps. The full target-camera assembly was mounted on a manual two-axis system for target displacement (see Fig. 2b).

2.3. Experimental characterization

The system characterization was carried out on February 17, 2023, from 13:01 to 14:12 (CET) at the Eduardo Torroja Institute for Construction Sciences (IETcc – CSIC) in Madrid, Spain, under sunny weather conditions. During the entire duration of the test, the Direct Normal Irradiance (DNI) was 980 ± 7 W m^{-2}, according to the data from the closest AEMET meteorological station in Madrid – Ciudad Universitaria.

The characterization methodology used is identical to previous studies [48,49,55–58]. The concentrated flux distribution on the Lambertian target was captured with the CCD camera, while the radiometer measured the received irradiance at a specific point. In a post-processing phase, the radiometer data and the CCD images were combined to convert the 8-bit grayscale image information to irradiance distributions. Owing to the high linearity of CCD sensor response to incident radiance, a strictly proportional relationship between grayscale and irradiance is expected. The proportionality coefficient is defined as the conversion factor (CF) that converts the grayscale values in bits (gs_i) of each “i” pixel of the image into irradiance values (I_i).

At the beginning of the campaign, the pixel size was determined using a calibration image of the target including a measuring tape reference. Knowing the pixel area (A_{px}) and CF, the total power (Q) on the target was assessed according to equation (1).

$$Q = A_{px} \cdot \sum_i I_i = A_{px} \cdot CF \cdot \sum_i gs_i \tag{1}$$

The average concentration factor (C_c) was then assessed for different circular and concentric areas around the maximum point. To calculate the average value for one circular region, the equation (2) was used:

$$C_c = \frac{\sum_1^n I_i}{DNI \cdot n} \tag{2}$$

where n indicates the number of pixels included in the region.

To quantify the theoretical maximum temperature achievable with a concentrated solar energy facility, the concept of stagnation temperature is often used [55]. Its value is obtained from an idealized radiative energy balance (see equation (3)).

$$T_s = \sqrt[4]{(q''/\sigma_{SB})} \tag{3}$$

Where q'' is the evaluated irradiance and σ_{SB} is the Stefan-Boltzmann constant.

In a second stage of the characterization, the distribution of the concentrated flux was assessed as the target was moved closer or further away from the lens. The displacement step between each position was 5 mm, and a total of 20 images were taken: 10 positions closer to the lens

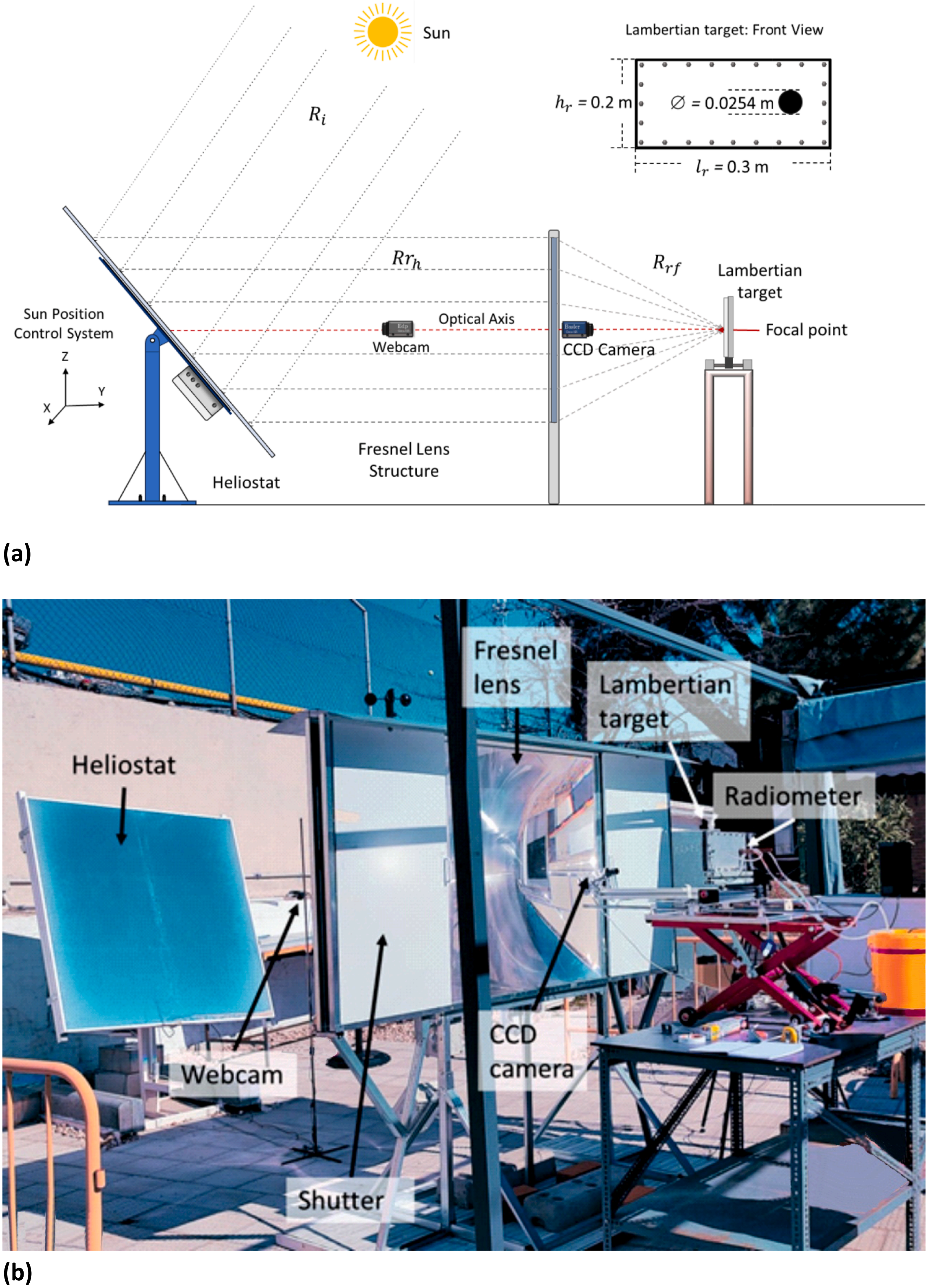

Fig. 2. Experimental setup for the solar furnace characterization: (a) schematic layout and (b) actual photograph.

and 10 positions farther away from the focal length. This mapping operation allows for the establishment of a 3D representation of incident flux isosurfaces.

In a third stage, the target was located again at the focal distance and the shutter was closed. The shutter doors were then slid into different positions, increasing the aperture by 10 cm each time, to assess the radiative power incident on the target.

The theoretical power that reaches the target can be calculated using equation (4):

$$Q_t = \rho_h \cdot \tau_l \cdot DNI \cdot A_l \tag{4}$$

where A_l is the illuminated surface of the lens. As mentioned earlier, the

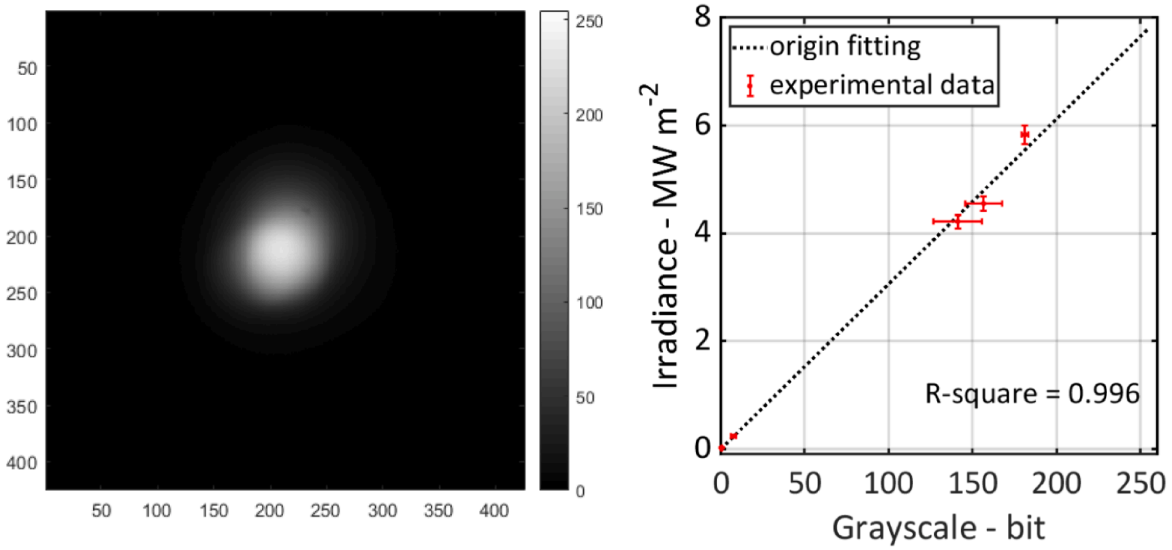

(a) **(b)**

Fig. 3. (a) Picture of the incident flux in grayscale intensity (8-bit). Size of the axes in pixels. (b) Conversion from grayscale to irradiance.

lens remained fully irradiated during the whole duration of the experiment and A_l depends only on the shutter position.

A Loss Factor (LF) was calculated as $LF = 1 - \frac{Q}{Q_t}$ for the different shutter apertures. This factor takes into account all the energy loss mechanisms in the system. These include soiling absorption and scattering on both the heliostat and the lens and shading due to the objects in the radiation path between the heliostat and the target (CCD camera and webcam for example).

2.4. Uncertainty analysis

Several sources of measurement uncertainty are considered. The radiometer suffers uncertainty from both the instrument itself (ε_r) and the DAQ system precision (ε_{DAQ}), as shown in equation (5).

$$\sigma_r = \sqrt{\varepsilon_r^2 + \varepsilon_{DAQ}^2} \tag{5}$$

The uncertainty associated with the grayscale values (σ_{gs}) in the CCD camera images depend on the radiometer's sensing area which cover several pixels(see equation (6)).

$$\sigma_{gs}^{rel} = \sqrt{\left(\frac{\sigma_{rc}}{\overline{gs}}\right)^2} \tag{6}$$

Subsequently, equations 7–11 are used to compute the uncertainty of the concentrated power that reaches the target. Equation (7) estimates the uncertainty related to the conversion factor CF:

$$\sigma_{CF} = \sqrt{\frac{\sum_i^m (Irr_i - CF \cdot gs_i)^2}{(m-2) \cdot \sum_i^m (gs_i - \overline{gs})^2}} \tag{7}$$

where m are the images used for the calibration, Irr_i is the irradiance measured by the radiometer when the image "i" was taken, gs_i is the average grayscale value of the pixels corresponding to the radiometer sensible area in the i image and $\overline{gs}$ is the mean grayscale value for these same gs_i values. The uncertainty on the pixel area ($\sigma_{A_{px}}$) is calculated with equation (8):

$$\sigma_{A_{px}} = 2 \cdot \frac{\sigma_{px}}{\overline{px}} \cdot A_{px} \tag{8}$$

where σ_{px} is the pixel side uncertainty, A_{px} is the pixel area and $\overline{px}$ is the mean value of the estimated pixel side. Equation (9) shows the uncertainty related to the sum of the gs_i values ($\sigma_{\sum gs_i}$), considering the standard deviation (σ_{gs_i}) for each of the n-pixels used for the total power calculation.

$$\sigma_{\sum gs_i} = \sqrt{\sum \sigma_{gs_i}^2} \tag{9}$$

The uncertainty on the total power ($\sigma_{Q_{FL}}$) is then assessed with equation (10).

$$\sigma_{Q_{FL}} = \sqrt{\left(\frac{\partial Q}{\partial A_{px}} \cdot \sigma_{A_{px}}\right)^2 + \left(\frac{\partial Q}{\partial CF} \cdot \sigma_{CF}\right)^2 + \left(\frac{\partial Q}{\partial (\sum gs_i)} \cdot \sigma_{\sum gs_i}\right)^2} \tag{10}$$

Finally, the uncertainty on the concentration factor (σ_{C_c}) was assessed with equation (11):

$$\sigma_{C_c} = \frac{1}{n} \cdot \sqrt{\left(\frac{\partial C_c}{\partial DNI} \cdot \sigma_{DNI}\right)^2 + \left(\frac{\partial C_c}{\partial CF} \cdot \sigma_{CF}\right)^2 + \left(\frac{\partial C_c}{\partial (\sum gs_i)} \cdot \sigma_{\sum gs_i}\right)^2} \tag{11}$$

where σ_{DNI} is the standard deviation of the DNI values recorded during the experiment.

3. Results

The target was first located at the theoretical focal length of 1000 mm and then moved until the smallest concentrated flux area was obtained leading to a real focal length of 993 mm. Fig. 3a shows the 8-bit grayscale image of the flux distribution at the real focal length. Thanks to the conversion obtained by the linear regression shown in Fig. 3b, the grayscale intensities were converted to irradiance values. The calculated conversion factor was approximately 30 kW m^{-2} bit^{-1} and the R-square from the linear regression was 0.996. The estimated uncertainties related to the radiometer ε_r and the DAQ system ε_{DAQ} were respectively 3 % and 1.1 % according to the suppliers' data.

Fig. 4a was obtained with a pixel size of 0.132 mm and shows a peak flux of approximately 7 MW m^{-2} with a relatively axisymmetric

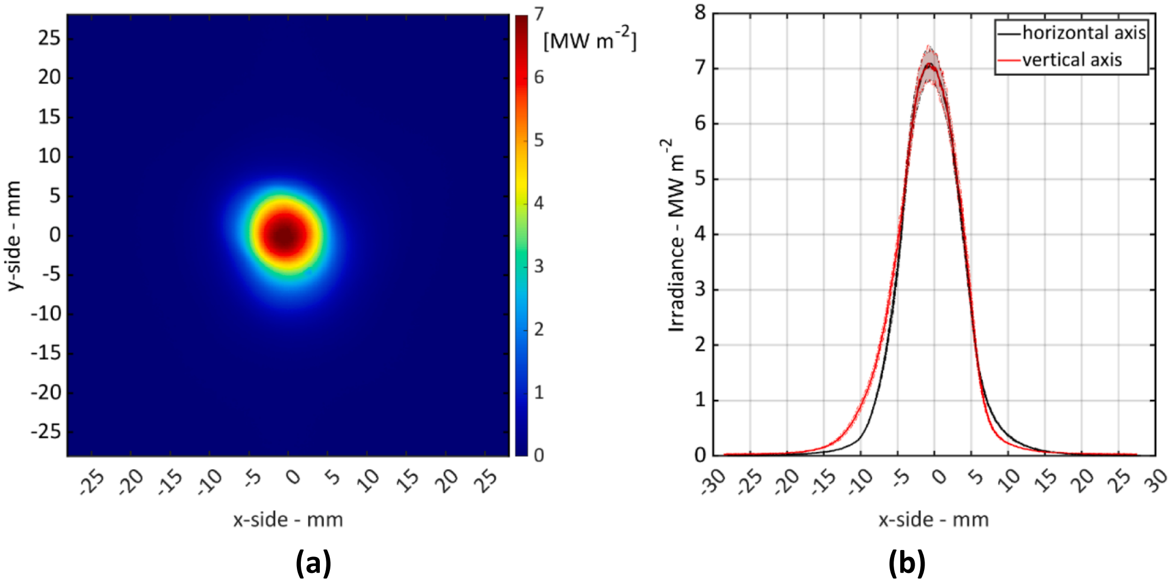

Fig. 4. (a) Solar furnace target flux distribution at the experimentally determined focal length. (b) Irradiance profiles along the horizontal and vertical axes passing through the flux distribution centroid.

irradiance distribution. In Fig. 4b the vertical and horizontal cross sections of the flux distribution show very similar Gaussian profiles. The total power (Q) calculated on the target was approximately 820 W. Fig. 5 displays the average solar concentration (C_c) and the power contained inside concentric circles of different radii around the centroid. At the focal distance, 50 % of the power is included in a 5 mm radius circle with a C_c of about 4500 suns and 90 % in a 13 mm radius circle with more than 1200 suns. For these concentrations and considering a DNI of 1 kW m^{-2}, equation (3) estimates stagnation temperatures of approximately 2700 and 1900 °C, respectively.

The theoretical power (Q_t) was estimated to 1025 W resulting in a loss factor of 0.2. As already mentioned, this parameter considers the losses due to soiling and the presence of objects blocking radiation in the optical path. Visual inspection showed appreciable levels of soiling and indicates that a significant improvement in performance could be achieved if careful cleaning of the heliostat and lens was performed periodically. Nevertheless, the results obtained from the experimental campaign comply with the initial requirements for the facility. Table 1 summarizes the main parameters obtained during the first stage of the campaign.

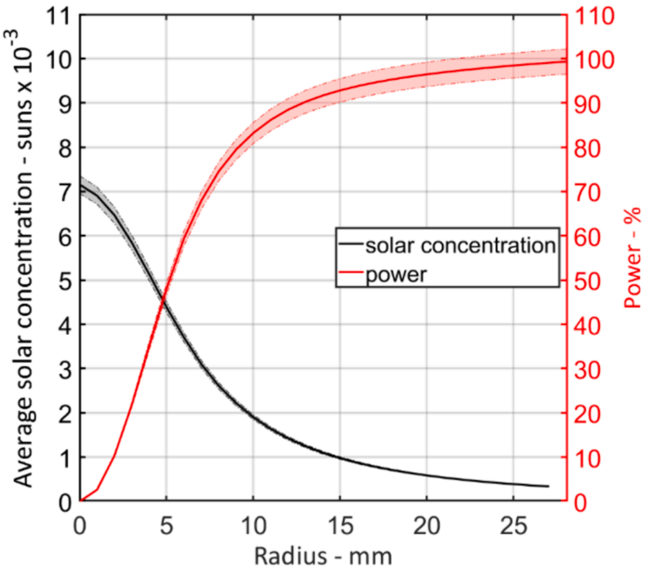

Fig. 5. Average solar concentration in concentric circles of different radii around the irradiance distribution centroid and the corresponding integrated incident power. The red shading indicates the uncertainty associated to the power estimation. (For interpretation of the references to colour in this figure legend, the reader is referred to the web version of this article.)

3.1. Flux distributions outside of the focal length

The second phase of the campaign was carried out to determine how the irradiance distribution changes along the optical axis of the lens, in the vicinity of the focal point. Fig. 6 shows flux maps obtained at distances of −35 mm (closer to the lens) to + 35 mm (away from the lens) from the focal length, in 5 mm increments. Distributions outside the −35 to + 35 mm range are not reported because peak irradiance are below 1 MW m^{-2} and resolution dropped significantly. As expected, the maximum irradiance decreases rapidly when the target is defocused. In addition, the distributions show an asymmetric behavior outside of the focal plane, with opposite elliptical deformations directions on either side of the focal plane, which could indicate some degree of optical misalignment and/or twisting in the heliostat or FL geometry. The small dark spot visible in many images of Fig. 6 is due to an imperfection on the target.

The irradiance distributions in Fig. 6 were used to create 3D isosurfaces which describe the locus of points with the same intensity. Fig. 7 illustrates their development around the focal length and reveal narrow shapes along the x and y axes with more elongation along the z axis as irradiance drops. This means that the receiver aperture must be carefully positioned at the focal point if the maximum level of concentration is to be achieved, but there could be some tolerance along the z

Table 1
Summary of main parameters obtained experimentally.

Parameter	Unit of measurement	Value	Uncertainty	Relative error
Focal length	mm	993	± 1	0.1 %
Total power	W	820	±23	2.8 %
Irradiance peak	MW m^{-2}	7.16	± 0.29	4.1 %
90 % power spot radius	mm	13.02	± 0.13	1.0 %
Loss factor	–	0.200	± 0.023	11.5 %

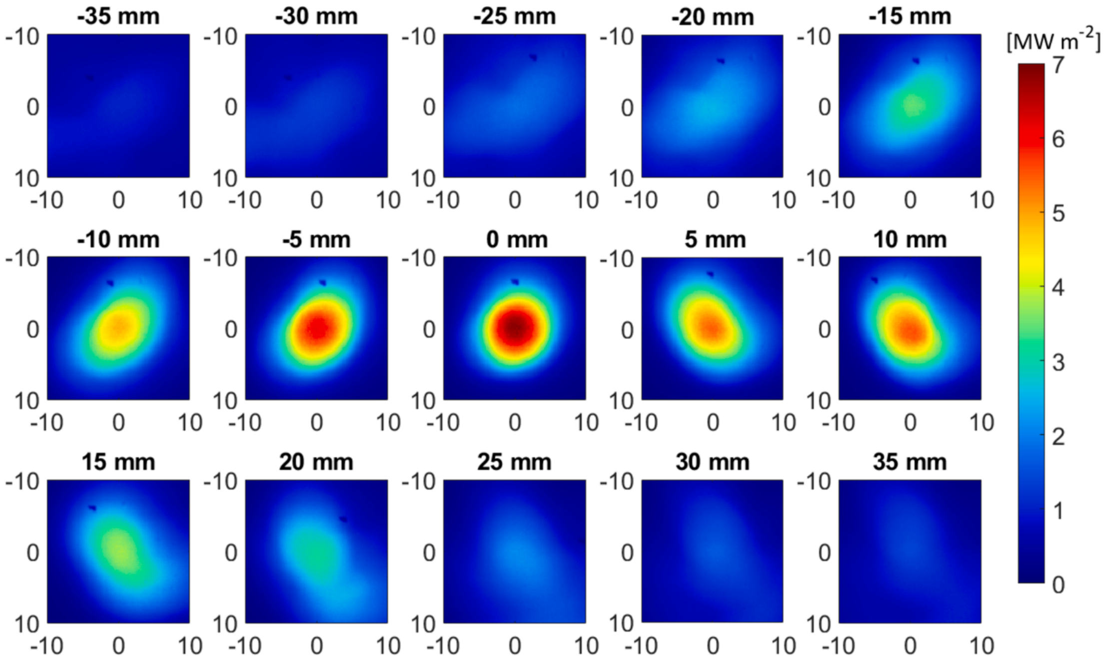

Fig. 6. Irradiance distributions in the vicinity of the focal plane, where 0 represents the focal length. The x and y axes are in mm.

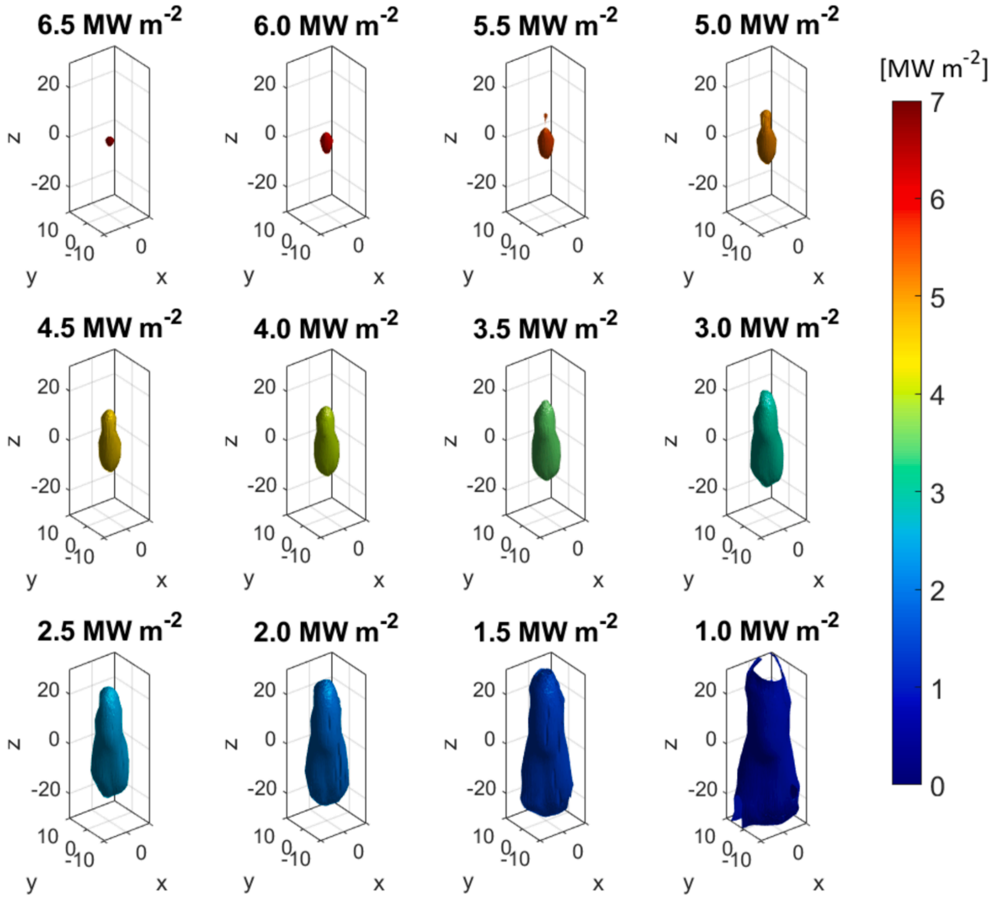

Fig. 7. Flux isosurfaces around the focal length position. The z-axis corresponds to the direction parallel to the lens optical axis. The x, y and z axes are in mm.

position of the receiver aperture if relatively modest irradiance levels are needed. Such isosurfaces can also be useful in designing receivers with tailored flux distributions.

3.2. Shutter characterization

In the third phase of the campaign, the influence of shutter operation on the FL-based furnace was measured. In Fig. 8a the horizontal cross section of the irradiance profiles obtained with different shutter apertures are depicted. The irradiance peaks vary from 1 MW m^{-2}, at 9 % aperture (distance of 100 mm between the two shutter doors), to almost 7 MW m^{-2} when the doors are fully open. The flux distribution gets larger and the peak irradiance higher as the shutter aperture increases. The total powers were computed by integrating the irradiance distribution in each plane.

Fig. 8b displays the changes in peak irradiance and total power as a function of shutter aperture. These values are compared with the maximum power and maximum peak irradiance for the full spot (100 % aperture). The power exhibits an almost linear relationship to shutter aperture, while the peak irradiance trend deviates from the proportionality. This discrepancy is due to several factors:

- The areas of the lens that are the furthest away from the optical axis contribute less to the peak flux at the center of the target than the central ones and therefore have a lower impact on peak flux as they get blocked by the shutter.
- The optical efficiency of the lens is not homogenous on the whole surface due to local thickness variations and deformations which, compounded with potential chromatic aberrations, may provoke deviations from a lineal behavior.
- The presence of the CCD camera and its support causes blockage in the central part of the lens.
- The presence of inhomogeneous soiling on both the heliostat and the lens.

Finally, the loss factor (*LF*) varies from 0.15 to 0.23 from the smallest to the largest apertures, with an average of 0.18 ± 0.02 which indicates that the central part of the FL, more protected by the shutter door when the system is not operating, was slightly cleaner than the edges.

4. Modeling and verification of experimental results

A ray tracing model was established to cross-check the experimental results and increase confidence into the high flux values observed. For this exercise, the open-source python–based *Tracer* code was used (https://github.com/casselineau/Tracer). Tracer is a fully object-oriented, general-purpose ray-tracer with a wide range of supported geometries and optical properties. In the absence of detailed information about several important factors (soiling levels for example), the simulation considers a relatively ideal situation, offering an upper-bound for performance estimation. The simulations results can then be used to assess if the experimental results are reasonably close to the model.

The model implements the detailed geometry of the FL, a single facet flat heliostat and a range of target planes positioned at the same location as considered in Fig. 6 to simultaneously measure the radiation passing through all targets in a single simulation. Since the actual shape of the lens grooves is not known, the theoretical design which is a 1 m focal length FL composed of 2200 conical teeth, framed in a square-shaped base is considered in the simulation. The material of the lens is PMMA and simulations are performed assuming a wavelength of 587.6 nm, in the region of average energy of the solar spectrum, for all rays for which

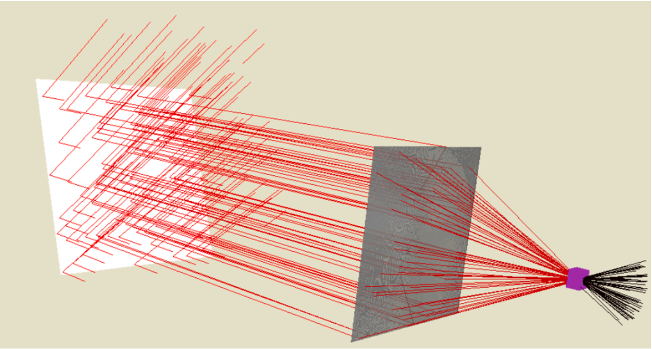

Fig. 9. Visual rendering of the ray-tracing simulation setup, highlighting the heliostat, the Fresnel lens, and the stack of flux-mapping targets (in purple). (For interpretation of the references to colour in this figure legend, the reader is referred to the web version of this article.)

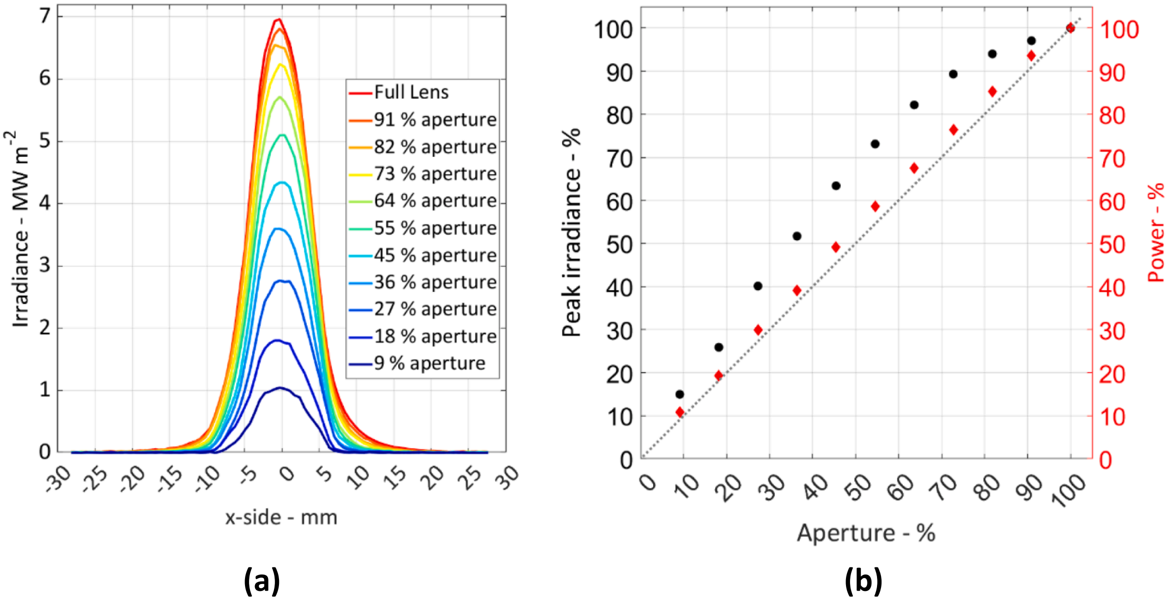

Fig. 8. (a) Irradiance profiles along the x-direction for a range of shutter apertures. (b) Percentages of peak irradiance (left axis) and total power (right axis) relative to the corresponding maximum obtained for the full spot for various shutter apertures.

the complex refractive index of PMMA is m = 1.49 + *i* 1.8e-7 [59]. Rays are deviated at the interface between air, assumed perfectly transparent with a refractive index of n = 1, and PMMA based on Fresnel's law of refraction, neglecting the influence of the coefficient of attenuation on the refracted angle owing to its small magnitude. For the solar resource, the simulation assumes a Buie sunshape [60] with 2 % CSR, including the polynomial correction introduced in [61]. Fig. 9 shows a 3D rendering of the ray-tracing scene considered.

The comparison between the simulation results and the experiments shows a relatively good agreement in terms of peak irradiance and power collected at the focal plane. However, deviations are noted when looking at the distribution of irradiance outside of the focal plane. Fig. 10 shows the simulated irradiance distribution at locations identical to the experimental measurements shown in Fig. 6. Unlike in the experimental dataset, simulated ideal irradiance distributions remain axis-symmetrical in all planes. In addition, irradiance reductions away from the focal plane is less pronounced (see Fig. 10) than in the experimental data (see Fig. 6).

The maximum irradiance is higher in the experimental cases (around 7 MW m^{-2}) than in the simulated ones (almost 6 MW m^{-2}) whereas the Gaussian-like distribution in the experimental results is narrower, as shown in Fig. 11a. The coefficient of determination, calculated by comparing the pixel values of the experimental and simulated irradiance distributions at the focal plane, is 0.90. These discrepancies are notable and could be due to the shape of the teeth and overall profile of the lens assumed in the model and which may not correspond to the real device. Hyperbolic profiles for the lens grooves could potentially increase solar concentration on the target and narrower distributions.

Furthermore, factors such as soiling, optical errors in the lens and in the heliostat due to local deformations can alter the results with respect to the theoretical ones. The spectral response of the lens, as well as the albedo of the surrounding surfaces, can also modify the irradiance on the target and these factors have not been taken into account in the simulations. Despite these differences, in the simulations, the total power received on a target of 100x100 mm located at the different planes is in good agreement with the theoretical one (approximately 95 %) as shown in Fig. 11b.

In Fig. 11b the experimental and simulated powers incident on a 20x20 mm target are also indicated for the planes located at the different position away from the focal length, while Table 2 shows the absolute and the relative error obtained by the comparison of those powers. Results indicate that the power collected on a 20x20 mm target is approximately 700 W for the planes located close to the focal length in both the experiments and simulations. The maximum power is found at different distances in the experiment and in the simulations, however, the relative error in the total power is less than 3.5 % for the planes from −10 to + 10 mm. These small deviations, beyond the optical errors mentioned above are caused by a mismatch between the experimental focal length (0.993 m) and the focal length used for the simulated lens geometry (1 m).

It is worth noting that the incident power on out-of-focus 20x20 mm targets drops more quickly in the experiments than in the model as the distance to the focus increases. As mentioned earlier, the model adopted near-ideal geometries and conditions and was expected to produce such over-performing results. Moreover, scattering by geometrical imperfections and soiling are suspected to cause wider flux distributions and spillage in the experiments. Overall, the findings of the simulations are consistent with higher experimental error. In conclusion, the model is successful in confirming the experimental work while highlighting some interesting and non-negligible discrepancies for out-of-focus flux distributions. Further work, outside of the scope of this study, is needed to understand precisely the source of said discrepancies.

5. Conclusion and future work

The investigation characterized a new Fresnel lens-based solar furnace at Eduardo Torroja Institute for Construction Sciences in Madrid, Spain, demonstrating that it meets initial requirements and resolves many issues found in existing installations. The furnace facilitates rapid experimental setup and is flexible, easy to operate, maintain, and has a low environmental impact. Key findings include:

- Total power of approximately 800 W and an average concentration of 1.2 MW m^{-2} in a 13 mm radius circle (90 % capture ratio).
- Record peak irradiance superior to 7 MW m^{-2} for a Fresnel lens solar furnace, enabling both high-temperature experiments (up to 2000 °C) and rapid execution times.

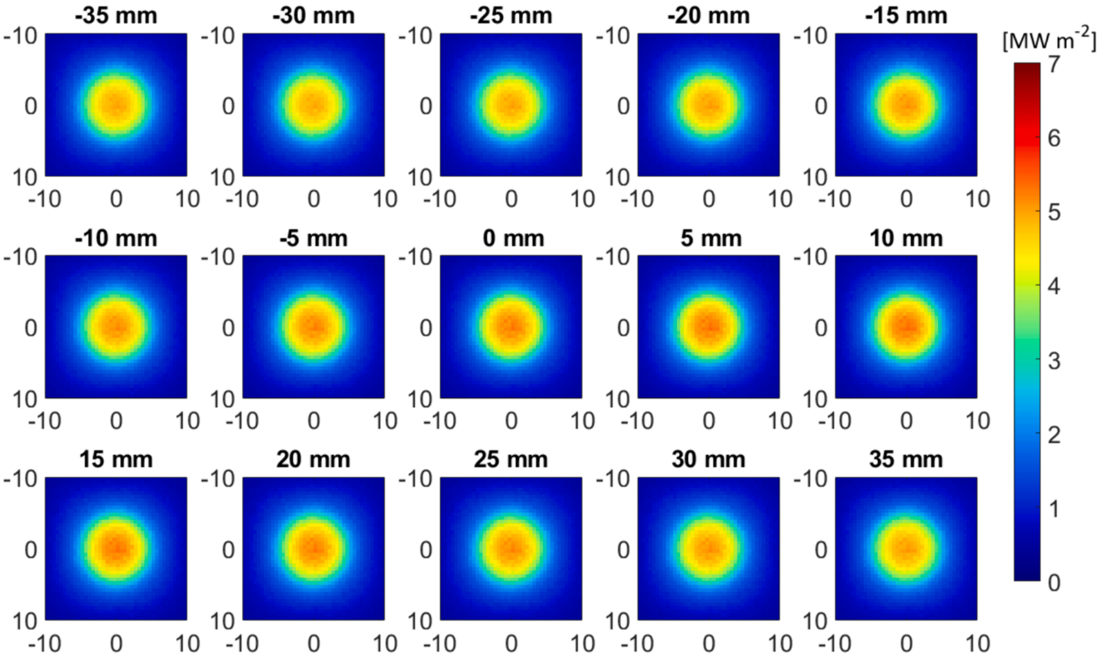

Fig. 10. Irradiance distributions on different planes parallel to the lens. 0 mm represents the focal length. The x and y axes of each distribution are in mm.

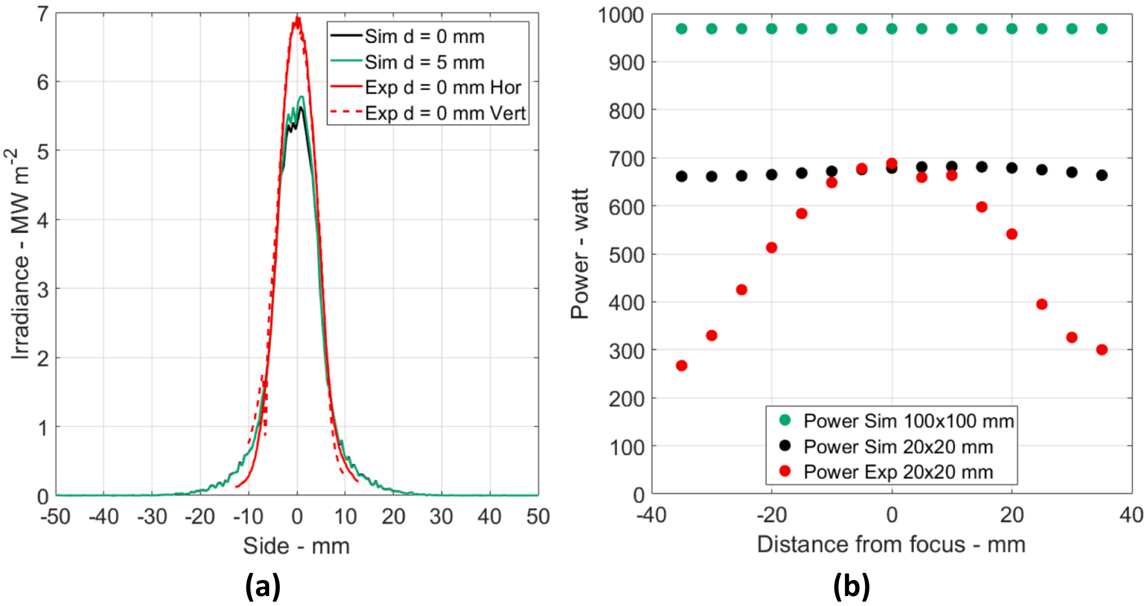

(a)

(b)

Fig. 11. (a) Comparison of simulated and experimental focal plane irradiance distributions along the horizontal and vertical directions. (b) Comparison of simulated and experimental incident powers on targets located at different distances from the lens (focal plane distance = 0 mm). The simulated incident power is calculated in a target region of 100x100 mm and 20x20 mm; experimental power is limited to a target region of 20x20 mm.

Table 2
Absolute and relative error for the total power in a 20x20 target region.

Distance from focal length [mm]	−35	−30	−25	−20	−15	−10	−5	0	5	10	15	20	25	30	35
Absolute error [W]	394	331	237	152	84	23	−2	−10	21	18	83	138	280	344	363.1
Relative error [%]	59.6	50.1	35.8	22.8	12.6	3.5	−0.3	−1.4	3.1	2.7	12.2	20.3	41.5	51.3	54.7

- Linear relationship between shutter opening and total power, allowing flexible power control over a wide range of irradiances (up to 5000 suns).
- The closed-loop control implemented in the heliostat tracking system ensures that solar radiation is always focused on the same point during operation.
- Ordinary maintenance basically consists of periodic cleaning of the flat surfaces of the heliostat and the Fresnel lens.
- Low-cost concentrator element at less than 300 USD per square meter, with easy replacement, making it a cost-effective solution for high solar flux prototype testing.

This facility will be used for high-temperature treatment of materials including construction and ceramic materials.

Declaration of Generative AI and AI-assisted technologies in the writing process

During the preparation of this work ChatGPT3.5 was used to improve the language quality and readability. After using this tool/service, the authors reviewed and edited the content as needed and take full responsibility for the content of the publication.

Declaration of competing interest

The authors declare that they have no known competing financial interests or personal relationships that could have appeared to influence the work reported in this paper.

Data availability

Data will be made available on request.

Acknowledgements

The authors express their gratitude to the Eduardo Torroja Institute for Construction Science for providing the location and entire infrastructure to enable the installation of this solar furnace. This infrastructure has been supported by the grant MAT2017–83025–R funded by MCIN/AEI/10.13039/501100011033.

A. Gallo wishes to thank the University of Almería for his Margarita Salas post-doctoral fellowship RR_A_2021_11 funded by the European Union within the framework of the "Recovery, Transformation and Resilience Plan" promoted by the Spanish government.

C.-A. Asselineau wishes to acknowledge the funding provided by the Ramón-y-Cajal fellowship grant RYC2022-038071-I funded by MICIU/AEI/10.13039/501100011033 and the ESF+.

Additionally, the authors extend their thanks to P. Pizarro (Green Oil Energy Systems SL) for his contribution during the design, procurement and construction of the facility.

References

[1] International Renewable Energy Agency (IRENA), Global Renewables Outlook: Energy transformation 2050, 2020.
[2] Solar Payback, Solar Heat for Industry, 2017. http://www.solrico.com/fileadmin/solrico/media/doc/Solar_payback/Solar_Heat_for_Industry_Solar_Payback_April_2017.pdf.
[3] M.J.S. Castellano, R.A.L. Quiroz, S. Taramona, A. Gallo, P. Contreras-Lallana, J. G. Hernández, Drying of Asphalt Plant Aggregates Using Concentrated Solar Energy, Proceedings - ISES Solar World Congress 2021 (2021) 620–630, https://doi.org/10.18086/swc.2021.26.06.
[4] R. Perez-Enciso, A. Gallo, D. Riveros-Rosas, E. Fuentealba-Vidal, C.A. Pérez-Rábago, A simple method to achieve a uniform flux distribution in a multi-faceted point focus concentrator, Renew Energy 93 (2016) 115–124, https://doi.org/10.1016/j.renene.2016.02.069.
[5] S. Taramona, A. Gallo, H. González-Camarillo, G. Minio Paluello, J.V. Briongos, J. Gómez-Hernández, Beam-down linear Fresnel reflector prototype : Construction

and first tests, Renew Energy 220 (2024), https://doi.org/10.1016/j.renene.2023.119697.

[6] E. Alonso, A. Gallo, M.I. Roldán, C.A. Pérez-Rábago, E. Fuentealba, Use of rotary kilns for solar thermal applications : Review of developed studies and analysis of their potential, Sol. Energy 144 (2017) 90–104, https://doi.org/10.1016/j.solener.2017.01.004.

[7] A. Gallo, M.I. Roldán, E. Alonso, E. Fuentealba, Considerations for using a rotary kiln for high temperature industrial processes with and without thermal storage, in: ISES EuroSun Conference, Palma de Mallorca (Spain), 2016. Doi: 10.18086/eurosun.2016.02.04.

[8] V. Kumar, R.L. Shrivastava, S.P. Untawale, Fresnel lens: A promising alternative of reflectors in concentrated solar power, Renew. Sustain. Energy Rev. 44 (2015) 376–390, https://doi.org/10.1016/j.rser.2014.12.006.

[9] P.D. Sonawane, V.K. Bupesh Raja, Concentrated solar energy in materials processing, Int. J. Ambient Energy 41 (2020) 1201–1207, https://doi.org/10.1080/01430750.2018.1493398.

[10] W.T. Xie, Y.J. Dai, R.Z. Wang, K. Sumathy, Concentrated solar energy applications using Fresnel lenses: A review, Renew. Sustain. Energy Rev. 15 (2011) 2588–2606, https://doi.org/10.1016/j.rser.2011.03.031.

[11] K. Awasthi, D.S. Reddy, M.K. Khan, Design of Fresnel lens with spherical facets for concentrated solar power applications, Int J Energy Res 44 (2020) 460–472, https://doi.org/10.1002/er.4947.

[12] M.M. Valmiki, P. Li, J. Heyer, M. Morgan, A. Albinali, K. Alhamidi, J. Wagoner, A novel application of a Fresnel lens for a solar stove and solar heating, Renew Energy 36 (2011) 1614–1620, https://doi.org/10.1016/J.RENENE.2010.10.017.

[13] S. Kiyaee, Y. Saboohi, A.Z. Moshfegh, A new designed linear Fresnel lens solar concentrator based on spectral splitting for passive cooling of solar cells, Energy Convers Manag 230 (2021) 113782, https://doi.org/10.1016/J.ENCONMAN.2020.113782.

[14] N.Y.J. Tan, X. Zhang, D.W.K. Neo, R. Huang, K. Liu, A. Senthil Kumar, A review of recent advances in fabrication of optical Fresnel lenses, J Manuf Process 71 (2021) 113–133, https://doi.org/10.1016/J.JMAPRO.2021.09.021.

[15] A. Cañadilla, A. Romero, G.P. Rodríguez, Sustainable Production of Powder Metallurgy Aluminum Foams Sintered by Concentrated Solar Energy, Metals (basel) 11 (2021) 1544, https://doi.org/10.3390/met11101544.

[16] A. Ferriere, G.P. Rodriguez, J.A. Sobrino, Flux distribution delivered by a Fresnel lens used for concentrating solar energy, Journal of Solar Energy Engineering, Transactions of the ASME 126 (2004) 654–660, https://doi.org/10.1115/1.1638783.

[17] A.R. Gupta, V.K. Rathod, Solar radiation as a renewable energy source for the biodiesel production by esterification of palm fatty acid distillate, Energy 182 (2019) 795–801, https://doi.org/10.1016/J.ENERGY.2019.05.189.

[18] A.R. Jensen, I. Sifnaios, G.P. Caringal, S. Furbo, J. Dragsted, Thermal performance assessment of the world's first solar thermal Fresnel lens collector field, Sol. Energy 237 (2022) 447–455, https://doi.org/10.1016/j.solener.2022.01.067.

[19] L. Jing, H. Liu, Y. Wang, W. Xu, H. Zhang, Z. Lu, Design and optimization of fresnel lens for high concentration photovoltaic system, International Journal of Photoenergy 2014 (2014), https://doi.org/10.1155/2014/539891.

[20] A. Hijazi, C. Boyadjian, M.N. Ahmad, J. Zeaiter, Solar pyrolysis of waste rubber tires using photoactive catalysts, Waste Manag. 77 (2018) 10–21, https://doi.org/10.1016/J.WASMAN.2018.04.044.

[21] D.G. Morris, A. López-Delgado, I. Padilla, M.A. Muñoz-Morris, Selection of high temperature materials for concentrated solar power systems: Property maps and experiments, Sol. Energy 112 (2015) 246–258, https://doi.org/10.1016/J.SOLENER.2014.09.050.

[22] T. Yabe, B. Bagheri, T. Ohkubo, S. Uchida, K. Yoshida, T. Funatsu, T. Oishi, K. Daito, M. Ishioka, N. Yasunaga, Y. Sato, C. Baasandash, Y. Okamoto, K. Yanagitani, 100 W-class solar pumped laser for sustainable magnesium-hydrogen energy cycle, J Appl Phys 104 (2008), https://doi.org/10.1063/1.2998981/343252.

[23] M.T.B.F. Sales, Solar powered desalination system using Fresnel lens, IOP Conf Ser Mater Sci Eng 162 (2016) 012002, https://doi.org/10.1088/1757-899X/162/1/012002.

[24] B.D. Tibúrcio, D. Liang, J. Almeida, D. Garcia, M. Catela, H. Costa, C.R. Vistas, Fresnel Lens Solar-Pumped Laser with Four Rods and Beam Merging Technique for Uniform and Stable Emission under Tracking Error Influence, Energies 2023, Vol. 16, Page 4815 16 (2023) 4815. Doi: 10.3390/EN16124815.

[25] M.P.B. Martins, C.E. Hori, M.A.S. Barrozo, L.G.M. Vieira, Solar Pyrolysis of Spirulina platensis Assisted by Fresnel Lens Using Hydrocalumite-Type Precursors, Energies (basel) 15 (2022) 7590, https://doi.org/10.3390/en15207590.

[26] S.I. Palomino-Resendiz, D.A. Flores-Hernández, N. Lozada-Castillo, L. Guzmán-Vargas, A. Luviano-Juárez, Design and implementation of a robotic active solar distiller based on a Fresnel concentrator and a photovoltaic system, Energy Convers Manag 166 (2018) 637–647, https://doi.org/10.1016/J.ENCONMAN.2018.04.069.

[27] NREL, Best Research-Cell Efficiencies, 2023.

[28] F. Karimi, H. Xu, Z. Wang, J. Chen, M. Yang, Experimental study of a concentrated PV/T system using linear Fresnel lens, Energy 123 (2017) 402–412, https://doi.org/10.1016/j.energy.2017.02.028.

[29] P.J. Sonneveld, G.L.A.M. Swinkels, B.A.J. van Tuijl, H.J.J. Janssen, J. Campen, G.P.A. Bot, Performance of a concentrated photovoltaic energy system with static linear Fresnel lenses, Sol. Energy 85 (2011) 432–442, https://doi.org/10.1016/j.solener.2010.12.001.

[30] K. Ryu, J.G. Rhee, K.M. Park, J. Kim, Concept and design of modular Fresnel lenses for concentration solar PV system, Sol. Energy 80 (2006) 1580–1587, https://doi.org/10.1016/j.solener.2005.12.006.

[31] X. Ma, R. Jin, S. Liang, H. Zheng, Ideal shape of Fresnel lens for visible solar light concentration, Optics Express, Vol. 28, Issue 12, Pp. 18141-18149 28 (2020) 18141–18149. Doi: 10.1364/OE.386599.

[32] W.T. Xie, Y.J. Dai, R.Z. Wang, Numerical and experimental analysis of a point focus solar collector using high concentration imaging PMMA Fresnel lens, Energy Convers Manag 52 (2011) 2417–2426, https://doi.org/10.1016/J.ENCONMAN.2010.12.048.

[33] V.M. Andreev, A.S. Vlasov, V.P. Khvostikov, O.A. Khvostikova, P.Y. Gazaryan, S.V. Sorokina, N.A. Sadchikov, Solar Thermophotovoltaic Converters Based on Tungsten Emitters, J Sol Energy Eng 129 (2007) 298–303, https://doi.org/10.1115/1.2734576.

[34] P. Ghorpade, B. Gadilohar, D. Pinjari, Y. Shinde, G. Shankarling, Concentrated solar radiation enhanced one pot synthesis of DES and N-Phenyl phthalimide, Sol. Energy 122 (2015) 1354–1361, https://doi.org/10.1016/J.SOLENER.2015.10.040.

[35] S. Deshpande, B. Gadilohar, Y. Shinde, D. Pinjari, A. Pandit, G. Shankarling, Energy efficient, clean and solvent free photochemical benzylic bromination using NBS in concentrated solar radiation (CSR), Sol. Energy 113 (2015) 332–339, https://doi.org/10.1016/J.SOLENER.2015.01.008.

[36] A.B. Patil, S.R. Lanke, K.M. Deshmukh, A.B. Pandit, B.M. Bhanage, Solar energy assisted palladium nanoparticles synthesis in aqueous medium, Mater Lett 79 (2012) 1–3, https://doi.org/10.1016/J.MATLET.2012.03.069.

[37] S.K.C. Sastry, N.L. Jadhav, S.B. Doltade, D.V. Pinjari, Effect of concentrated solar radiation on the morphology of the silver nanoparticles and its antibacterial activity, Indian Chem. Eng. 61 (2019) 374–386, https://doi.org/10.1080/00194506.2019.1579674.

[38] A.R. Gupta, A.P. Jalan, V.K. Rathod, Solar energy as a process intensification tool for the biodiesel production from hempseed oil, Energy Convers Manag 171 (2018) 126–132, https://doi.org/10.1016/J.ENCONMAN.2018.05.050.

[39] R. Michalsky, P.H. Pfromm, Chromium as reactant for solar thermochemical synthesis of ammonia from steam, nitrogen, and biomass at atmospheric pressure, Sol. Energy 85 (2011) 2642–2654, https://doi.org/10.1016/J.SOLENER.2011.08.005.

[40] G. Herranz, A. Romero, V. de Castro, G.P. Rodríguez, Processing of AISI M2 high speed steel reinforced with vanadium carbide by solar sintering, Materials & Design (1980-2015) 54 (2014) 934–946. Doi: 10.1016/J.MATDES.2013.09.027.

[41] G. Herranz, A. Romero, V. De Castro, G.P. Rodríguez, Development of high speed steel sintered using concentrated solar energy, J Mater Process Technol 213 (2013) 2065–2073, https://doi.org/10.1016/j.jmatprotec.2013.06.002.

[42] C. Sierra, A.J. Vásquez, High solar energy concentration with a Fresnel lens, J Mater Sci 40 (2005) 1339–1343.

[43] M.A. Mazo, I. Padilla, A. López-Delgado, A. Tamayo, J. Rubio, Silicon Oxycarbide and Silicon Oxycarbonitride Materials under Concentrated Solar Radiation, Materials 14 (2021) 1013, https://doi.org/10.3390/ma14041013.

[44] I. Padilla, A. López-Delgado, S. López-Andrés, M. Álvarez, R. Galindo, A. J. Vazquez-Vaamonde, The application of thermal solar energy to high temperature processes: Case study of the synthesis of alumina from boehmite, Scientific World Journal 2014 (2014), https://doi.org/10.1155/2014/825745.

[45] A. López-Delgado, S. López-Andrés, I. Padilla, M. Alvarez, R. Galindo, A. J. Vázquez, Dehydration of Gypsum Rock by Solar Energy: Preliminary Study, Geomaterials 4 (2014) 82–91, https://doi.org/10.4236/GM.2014.43009.

[46] M.A. Mazo, I. Padilla, A. Tamayo, J.I. Robla, A. López-Delgado, J. Rubio, Evaluation of thermal shock resistance of silicon oxycarbide materials for high-temperature receiver applications, Sol. Energy 173 (2018) 256–267, https://doi.org/10.1016/J.SOLENER.2018.07.080.

[47] J. Zeaiter, M.N. Ahmad, D. Rooney, B. Samneh, E. Shammas, Design of an automated solar concentrator for the pyrolysis of scrap rubber, Energy Convers Manag 101 (2015) 118–125, https://doi.org/10.1016/J.ENCONMAN.2015.05.019.

[48] N. Estremera-Pedriza, J. Fernández-Reche, J.A. Carballo, Optical Characterization of a New Facility for Materials Testing under Concentrated Wavelength-Filtered Solar Radiation Fluxes, Solar 3 (2023) 76–86, https://doi.org/10.3390/solar3010007.

[49] N. Zhao, Z. Wu, H. Gao, S. Yan, X. Zhao, N. Zhang, T. Ming, Experimental analysis of the optical loss of a dusty Fresnel lens with a novel solar flux test system, Sustainable Energy Technol. Assess. 48 (2021), https://doi.org/10.1016/j.seta.2021.101656.

[50] I. Reda, A. Andreas, Solar position algorithm for solar radiation applications, Sol. Energy 76 (2004) 577–589, https://doi.org/10.1016/J.SOLENER.2003.12.003.

[51] H. González-Camarillo, R. Calleja, R.A. Pérez-Enciso, C.A. Pérez-Rábago, C.A. Estrada-Gasca, Corrección De La Deriva En Sistemas De Seguimiento Solar A Través De Control De Lazo Cerrado, in: CIES2020 - XVII Congresso Ibérico e XIII Congresso Ibero-Americano de Energia Solar, 2020: pp. 1–9.

[52] Meiying Optics, Large Fresnel Lens, (2022). https://www.meiyingoptics.com/sale-14183008-1100-1100mm-large-fresnel-lens-spot-fresnel-lens-big-fresnel-lens-pmma-fresnel-lens-for-solar-concen.html (accessed April 13, 2024).

[53] D. Codd, A. Carlson, J. Rees, A. Slocum, A Low Cost High Flux Solar Simulator, MIT Open Access Article, 2010.

[54] E.D. Thalhammer, G.S. Phipps, Heliostat beam characterization system., in: 25. ISA International Instrumentation Symposium, Anaheim, CA, USA, n.d.

[55] A. Gallo, A. Marzo, E. Fuentealba, E. Alonso, High flux solar simulators for concentrated solar thermal research: A review, Renew. Sustain. Energy Rev. 77 (2017) 1385–1402, https://doi.org/10.1016/j.rser.2017.01.056.

[56] A. Gallo, A.N. Castuera, Characterization of a Lambertian target, in: XII National and III International Conference on Engineering Thermodynamics - CNIT 12, Madrid, 2022: pp. 1–8.

[57] A. Gallo, H. González-Camarillo, M.I. Roldán, E. Alonso, C.A. Pérez-Rábago, Thermal Behavior and Heat-Flux Distribution in a Solar Rotary Kiln, in: SolarPaces Conference, 2017: pp. 1–8. Doi: 10.1063/1.5067157.

[58] J. Ballestrín, M. Casanova, R. Monterreal, J. Fernández-Reche, E. Setien, J. Rodríguez, J. Galindo, F.J. Barbero, F.J. Batlles, Simplifying the measurement of high solar irradiance on receivers, Application to Solar Tower Plants, Renew Energy 138 (2019) 551–561, https://doi.org/10.1016/j.renene.2019.01.131.

[59] X. Zhang, J. Qiu, J. Qiu, J. Qiu, X. Li, X. Li, J. Zhao, J. Zhao, L. Liu, L. Liu, Complex refractive indices measurements of polymers in visible and near-infrared bands, Applied Optics, Vol. 59, Issue 8, Pp. 2337-2344 59 (2020) 2337–2344. Doi: 10.1364/AO.383831.

[60] D. Buie, A.G. Monger, C.J. Dey, Sunshape distributions for terrestrial solar simulations, Sol. Energy 74 (2003) 113–122, https://doi.org/10.1016/S0038-092X(03)00125-7.

[61] C.-A. Asselineau, Geometrical Optimisation of Receivers for Concentrating Solar Thermal Systems, 2018.